World Academy of Science, Engineering and Technology
International Journal of Geological and Environmental Engineering
Vol:6, No:11, 2012

Development of Coronal Field and Solar Wind Components for MHD Interplanetary Simulations

Ljubomir Nikolić, Larisa Trichtchenko

Abstract—The connection between solar activity and adverse phenomena in the Earth's environment that can affect space and ground based technologies has spurred interest in Space Weather (SW) research. A great effort has been put on the development of suitable models that can provide advanced forecast of SW events. With the progress in computational technology, it is becoming possible to develop operational large scale physics based models which can incorporate the most important physical processes and domains of the Sun-Earth system. In order to enhance our SW prediction capabilities we are developing advanced numerical tools. With operational requirements in mind, our goal is to develop a modular simulation framework of propagation of the disturbances from the Sun through interplanetary space to the Earth. Here, we report and discuss on the development of coronal field and solar wind components for a large scale MHD code. The model for these components is based on a potential field source surface model and an empirical Wang-Sheeley-Arge solar wind relation.

Keywords—Space weather, numerical modeling, coronal field, solar wind.

I. Introduction

The scientific roots of Space Weather (SW) research go back to the first systematic studies of sunspots in the early 17^{th} century, to the discovery of large magnetic needle fluctuations by George Graham in 1724, and to the observation of solar flares in 1859. However, it took more than 100 years from the first evident observation that occurrence of aurora is connected to the disruption of telegraphic services in March 1847, to establish connection between solar activity and phenomena in the Earth's environment. Important missing links in the Sun-Earth chain were closed by Eugene Parker's solar wind theory in the 1950's [1] and discovery of Coronal Mass Ejections (CME) in 1971 [2]. Collapse of Hydro-Quebec power grid in 1989 and the loss of Telstar satellite in 1997 are some examples of the events that spurred research interest in Sun-to-Earth physical processes and their effects. The fact that solar activity can pose a hazard and can have a major impact on modern society has prompted establishment of research and operational strategies to understand and predict SW [3]-[5].

Today, the term "Space Weather" refers to variable conditions in our space environment which can affect human activities, space and ground based technologies. Since human well-being is increasingly dependent on modern technology there is an upsurge of interest in the SW services including: government agencies, power-grid companies, aviation, pipeline operators and GNSS users. Canada, with its unique geographic location is particularly vulnerable to the SW effects. The Canadian SW Center, hosted at the Geomagnetic Laboratory, Natural Resources Canada (NRCan) in Ottawa with support from the Canadian Space Agency (CSA) monitors solar activity and parameters in the Sun-Earth system and provides information about the SW conditions [6].

A step forward in understanding SW phenomena occurred when a number of satellites were launched in the 1990s, improving our understanding of Sun's activity and phenomena in the Earth's environment. Unfortunately, the most reliable observations, from the L1 point, allow only $\sim$ 1h advanced warning of approaching solar disturbances. To achieve more advanced notifications, the SW research and operations heavily depend on development of numerical models. More efforts should be put to improve modelling capabilities, physics of the models, and in particular, to transfer simulation codes into operations [3]-[5].

Models such as semi-empirical Wang-Sheeley-Arge (WSA), Hakamada-Akasofu-Fry model (HAF), Shock Time of Arrival (STOA) and Interplanetary Shock Propagation Model (ISPM) are used in SW operations to predict solar wind speed (WSA, HAF) and arrival time of interplanetary shocks (HAF, STOA, ISPM) at 1AU [7]-[9]. These models utilize a class of empirical rules that transform real time observations into prediction of phenomena. In terms of computational requirements and complexity these models offer a great advantage over fully physics based models. However, the absence of clear physics often leads to prediction inaccuracy especially in the case of violent solar disturbances. For example, the predictions of the HAF, STOA and ISPM models often reveal a more than 12h discrepancy in the shock arrival time [10].

It is clear that improvements in the SW forecast can only be achieved using advanced numerical codes that treat plasma and fields self-consistently. Despite the fact that fully physics based simulations, in particular MHD, have been used in academic research since the early 1980s, the implementation of these codes into SW operations poses a challenge, ranging from computational constraints to the lack of observational data that can be used to deduce code-relevant input parameters. Furthermore, the majority of the scientific codes were not designed with operational functionality in mind and thus require significant changes in the code structure. Recently, the ENLIL code [11] has been implemented at NOAA as the first large scale MHD SW operational code [12] that provides 1-4 day advanced warning of shock arrivals. The code uses the WSA model for the background solar wind and a cone model for the CME initiation.

The Canadian Space Weather Center is trying to enhance its prediction capabilities using modern numerical approaches as

Lj. Nikolić and L. Trichtchenko are with Geomagnetic Laboratory, Natural Resources Canada, 7 Observatory Crescent, Ottawa, ON, K1A 0Y3, Canada (e-mail: ljubomir.nikolic@nrcan-rncan.gc.ca).

well. With SW operational requirements in mind, our goal is to develop a modular simulation framework for the propagation of solar disturbances through interplanetary space. Modularity of the framework should ensure easy extensions to incorporate new components. Here we report on our efforts and findings on the development of coronal magnetic field and solar wind components that will provide initial parameters for a MHD simulation code. In section 1 we describe the governing equations used to transform observations of photospheric magnetic fields to construct global coronal fields and to determine quantities relevant to an empirical solar wind relation. In section 2 we present and discuss our results, and in section 3 we summarize our work.

II. Governing Equations of the Models

A. Coronal Fields

In this paper we use a potential field source surface model (PFSS) to derive global magnetic field **B** of the solar corona from photospheric field observations [13], [14]. The PFSS model assumes existence of a fixed spherical "source surface" where the coronal magnetic field is purely radial. A radius of $R_s = 2.5R_0$ for the source surface, where R_0 is the radius of the Sun, is widely accepted for the modelling. Although the fixed spherical surface assumption, together with the neglecting of coronal currents, poses a shortcoming of the PFSS model, the more exact solution using MHD approach does not offer significant advantage. It has been found that PFSS and MHD models give similar topology of the coronal magnetic field [15]. However, the PFSS has a significant advantage in respect to complexity and computational time. Here, we outline the main steps to derive the PFSS based solution.

To start, it is assumed that there are no currents in the region $R_0 \leq r \leq R_s$, which means that the magnetic field can be expressed as the gradient of a scalar potential Ψ

$$\nabla \times \mathbf{B} = 0 \;\; \Rightarrow \;\; \mathbf{B} = -\nabla\Psi, \tag{1}$$

which with the divergenceless property of the magnetic field

$$\nabla \cdot \mathbf{B} = 0, \tag{2}$$

gives Laplace equation for the potential

$$\nabla^2\Psi = 0. \tag{3}$$

Using the separation of variables $\Psi(r,\theta,\phi) = R(r)\Theta(\theta)\Phi(\phi)$ in the spherical coordinates, where $\theta \in [0,\pi]$ and $\phi \in [0,2\pi]$, and assuming that at the source surface $r = R_s$ the magnetic field is radial, i.e. $\Psi(R_s,\theta,\phi) = const.$, we can express the solution of (3) in the region $R_0 \leq r \leq R_s$ in terms of spherical harmonics as

$$\begin{aligned}\Psi &= \sum_{n=1}^{\infty}\sum_{m=0}^{n} P_n^m(\cos\theta)(g_{nm}\cos m\phi + h_{nm}\sin m\phi) \\ &\times \left[R_0\left(\frac{R_0}{r}\right)^{n+1} - R_s\left(\frac{R_0}{R_s}\right)^{n+2}\left(\frac{r}{R_s}\right)^{n}\right].\end{aligned} \tag{4}$$

Using (1) and (4) we can obtain the magnetic filed components:

$$\begin{aligned}B_r &= -\frac{\partial\Psi}{\partial r} = \sum_{n=1}^{\infty}\sum_{m=0}^{n} P_n^m(\cos\theta) \\ &\times (g_{nm}\cos m\phi + h_{nm}\sin m\phi) \\ &\times \left[(n+1)\left(\frac{R_0}{r}\right)^{n+2} + n\left(\frac{R_0}{R_s}\right)^{n+2}\left(\frac{r}{R_s}\right)^{n-1}\right],\end{aligned} \tag{5}$$

$$\begin{aligned}B_\theta &= -\frac{1}{r}\frac{\partial\Psi}{\partial\theta} = -\sum_{n=1}^{\infty}\sum_{m=0}^{n} \frac{\partial P_n^m(\cos\theta)}{\partial\theta} \\ &\times (g_{nm}\cos m\phi + h_{nm}\sin m\phi) \\ &\times \left[\left(\frac{R_0}{r}\right)^{n+2} - \left(\frac{R_0}{R_s}\right)^{n+2}\left(\frac{r}{R_s}\right)^{n-1}\right],\end{aligned} \tag{6}$$

$$\begin{aligned}B_\phi &= -\frac{1}{r\sin\theta}\frac{\partial\Psi}{\partial\phi} = \sum_{n=1}^{\infty}\sum_{m=0}^{n} P_n^m(\cos\theta) \\ &\times \frac{m}{\sin\theta}(g_{nm}\sin m\phi - h_{nm}\cos m\phi) \\ &\times \left[\left(\frac{R_0}{r}\right)^{n+2} - \left(\frac{R_0}{R_s}\right)^{n+2}\left(\frac{r}{R_s}\right)^{n-1}\right],\end{aligned} \tag{7}$$

where $P_n^m(\cos\theta)$ represent the associated Legendre polynomials. Multiplying (5) with $P_k^l(\cos\theta)\cos l\phi$ and $P_k^l(\cos\theta)\sin l\phi$ in the case $r = R_0$, the coefficients g_{nm} and h_{nm} in (4)-(7) can be found using orthogonality of the Legendre polynomials

$$\begin{aligned}&\int_0^{\pi}\sin\theta d\theta\int_0^{2\pi} d\phi P_n^m(\cos\theta)\left\{\begin{array}{c}\cos m\phi\\ \sin m\phi\end{array}\right\} \\ &\times P_k^l(\cos\theta)\left\{\begin{array}{c}\cos l\phi\\ \sin l\phi\end{array}\right\} = \frac{4\pi}{2n+1}\delta_{nk}\delta_{ml},\end{aligned} \tag{8}$$

where we use Schmidt normalization. Thus we have

$$\begin{aligned}\left\{\begin{array}{c}g_{nm}\\ h_{nm}\end{array}\right\} &= \frac{2n+1}{4\pi\left(n+1+n\left(\frac{R_0}{R_s}\right)^{2n+1}\right)}\int_0^{\pi}\sin\theta d\theta \\ &\times\int_0^{2\pi} d\phi B_r(R_0,\theta,\phi)P_n^m(\cos\theta)\left\{\begin{array}{c}\cos m\phi\\ \sin m\phi\end{array}\right\}.\end{aligned} \tag{9}$$

Since the radial component of the photospheric magnetic field $B_r(R_0,\theta,\phi)$ in (9) can be derived from the solar magnetograms, using (5)-(7) we can now construct magnetic field in the region $R_0 \leq r \leq R_s$. To expand the fields beyond the source surface R_s, one can utilize the Schatten current sheet model [16].

B. Solar Wind

Two parameters that can be calculated from the coronal field play an important role in the solar wind speed V_{sw}. It has been found [7], [8] (WSA model), that the flux tube expansion factor

$$f_s = \frac{|\mathbf{B}(R_0)|}{|\mathbf{B}(R_s)|}\frac{R_0^2}{R_s^2}, \tag{10}$$

and the angular separation between a magnetic field foot point and the coronal hole boundary θ_b at the photosphere, are well

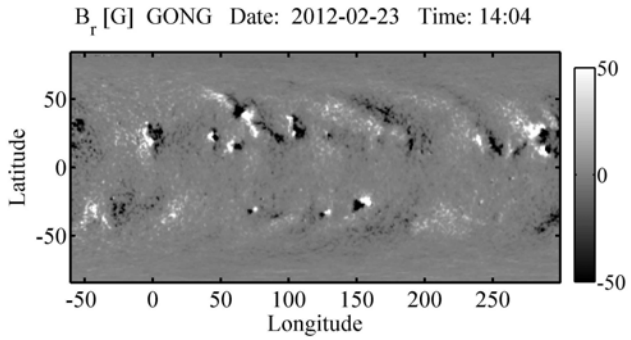

Fig. 1. Observed photospheric radial component of the magnetic field $B_r(R_0, \theta, \phi)$ from the GONG synoptic magnetogram. The longitude 0° corresponds to the central meridian on February 23, 2012 (14:04UT). The left side from the central meridian is towards the east of the Sun. The magnetic field scale is saturated at ± 50G.

correlated with the solar wind speed. There are several forms of empirical relations that connect f_s and θ_b with V_{sw}. A general form of the relation can be expressed [17] as,

$$V_{sw}\left[\frac{\mathrm{km}}{\mathrm{s}}\right] = a_1 + \frac{a_2}{(1+f_s)^{a_3}}\left[a_4 - a_5 \exp\left\{-\left(\frac{\theta_b}{a_6}\right)^{a_7}\right\}\right]^{a_8}, \quad (11)$$

where a_1-a_8 are empirical numerical coefficients. These coefficients are tunable parameters that depend on the magnetogram source used to derive the coronal magnetic field, resolution, radius of the surface where the solar wind is calculated, etc.

III. Results and Discussion

We have developed a modular numerical Fortran code for the magnetogram processing and calculation of the coronal field based on the PFSS model. As the input to the code, we use synoptic magnetograms to obtain the observed radial component of the magnetic field. There are several sources of full rotation maps of the photospheric field. In this paper we use hourly-updated standard GONG synoptic magnetograms [18]. These magnetograms are provided in the FITS format with the $180 \times 360\ \sin(\theta) - \phi$ grid. Here θ denotes the latitude and ϕ represents the longitude.

With the help of cfitsio library [19] for reading the files, we remesh the magnetograms to a uniform latitude-longitude grid. In Fig. 1 we show a GONG hourly-updated classic synoptic magnetogram. To better represent the details, the magnetic field scale is saturated in Fig. 1 at ± 50G. The longitude 0° corresponds to the central meridian on February 23, 2012 (14:04UT). The region on the left side of the central meridian is the region that will cross the meridian in coming days after 23^{rd}. Using $B_r(R_0)$ from this synoptic map we can obtain harmonic coefficients g_{nm} and h_{nm}. To calculate this we use a discretized form of (9). We note that the discretization is limited by the magnetogram resolution. We have compared our calculated harmonic coefficients with Luhmann's coefficients [18] and a good agreement has been found.

The radial magnetic field (5) obtained using harmonic expansion should match the magnetic field of the original magnetogram (Fig. 1) for $r = R_0$. In Fig. 2 we show the

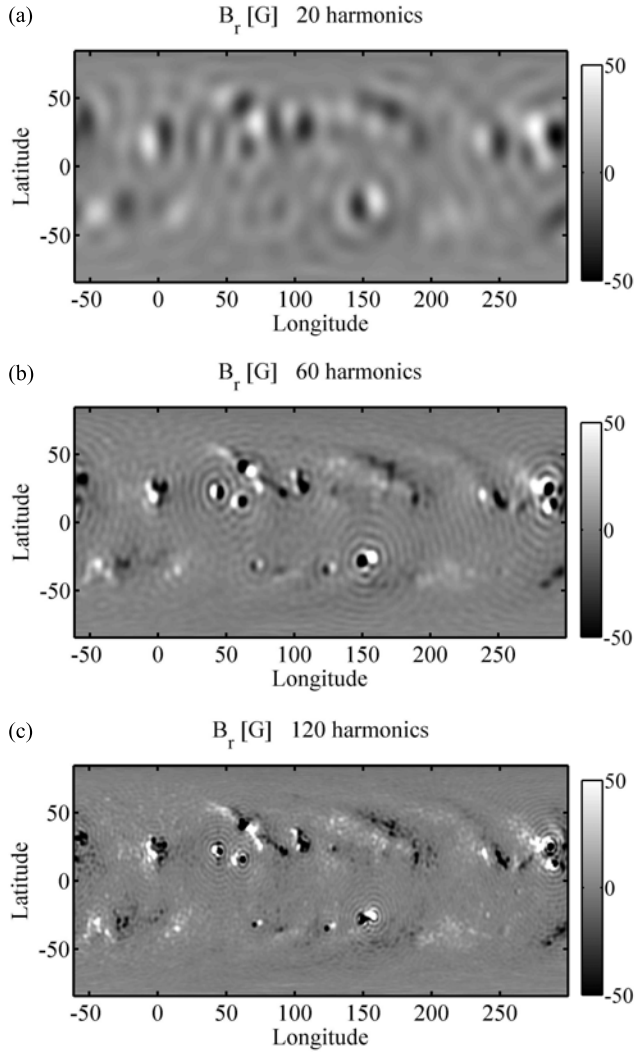

Fig. 2. Photospheric radial component of the magnetic field $B_r(R_0, \theta, \phi)$ calculated with (a) $n_{max} = 20$, (b) $n_{max} = 60$, and (c) $n_{max} = 120$. The magnetic field scale is saturated at ± 50G.

results of the calculation of $B_r(R_0, \theta, \phi)$ with a different number of harmonics limited by $n \leq n_{max}$. In a number of PFSS magnetic field derivations a low number of harmonics has been used (typically $n_{max} < 20$). However, as we can see from the comparison of Fig. 1 and Fig. 2, the fine details are blurred for $n_{max} = 20$ (Fig. 2a), and the result does not represent well the observed field. Another problem which is not so apparent in Fig. 2a is clearly visible in Fig 2b. Although the increase of the degree of the harmonic functions to $n_{max} = 60$ improves the quality of the details, the result also reveals a shortcoming of the PFSS model. A series of ring-like structures surrounding the active regions can be seen in Fig. 2b. This known effect is induced by a large abrupt difference in the observed magnetic field intensity in the active regions (see [20]). Therefore, the ringing effect is more pronounced on magnetograms with strong active regions than in the case of "quiet" magnetograms. Using more harmonics can decrease the artifacts. As we can see from Fig. 3 using $n_{max} = 120$ we can reproduce the original magnetogram from

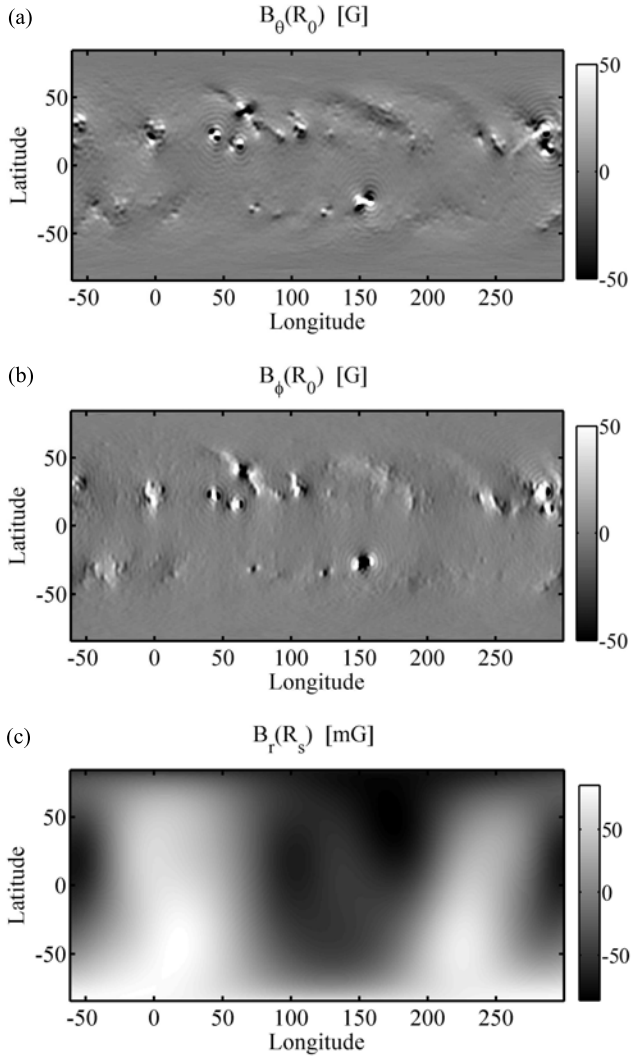

Fig. 3. Solution for the photospheric magnetic field components (a) B_θ and (b) B_ϕ with $n_{max} = 120$. The magnetic field scale is saturated at $\pm$50G. (c) Solution for the radial component of the magnetic field B_r at source surface R_s with $n_{max} = 120$.

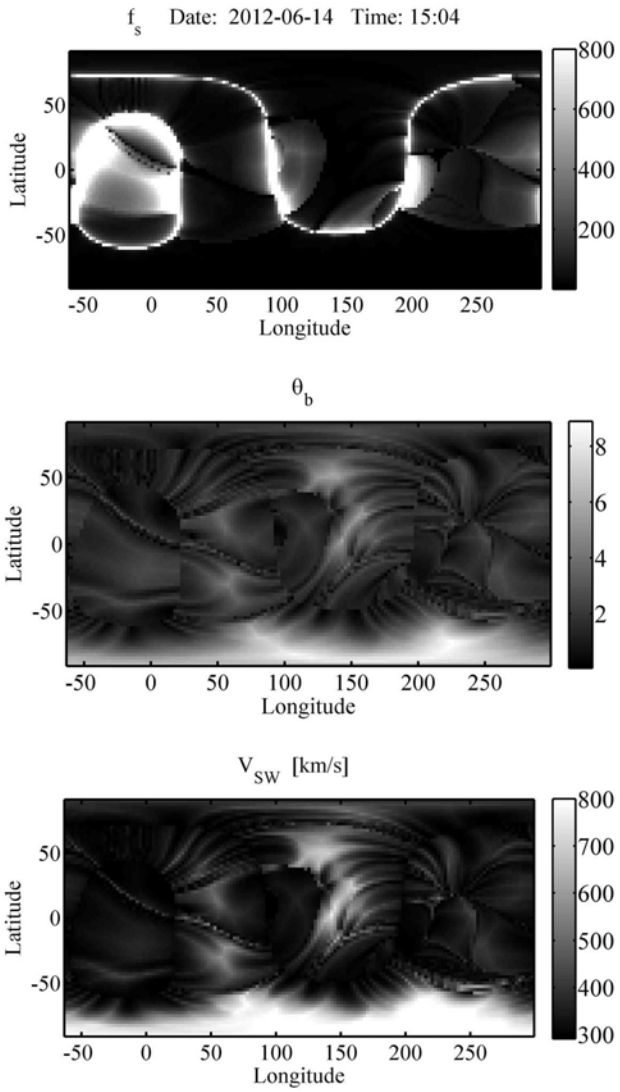

Fig. 4. (a) Magnetic flux tube expansion factor f_s, (b) nearest coronal hole boundary factor θ_b, and (c) solar wind speed V_{sw} at R_s. The synoptic magnetogram used as the input for the code is from June 14, 2012 (15:04UT).

Fig. 1 very well. However, we should point out that using too many harmonics can lead to the generation of artificial magnetic fields, in particular in the polar regions.

Using the PFSS equations (5)-(7) we can now derive a full 3D coronal magnetic field. In Fig. 3 we show the result for the magnetic field calculated with $n_{max} = 120$ to minimize the ringing effect. We use magnetogram from Fig. 1 as the input for the code. In Fig. 3a and 3b, we show a photospheric map of B_θ and B_ϕ, respectively, with the magnetic field scale saturated at $\pm$50G. In Fig. 3c we plot the solution for the radial component of the magnetic field B_r at the source surface. The calculated B_θ and B_ϕ components vanish at R_s, in agreement with the definition of the source surface.

Once the distribution of the magnetic field in the solar corona is known, we can trace the magnetic field lines using the following equations:

$$\frac{dr}{ds} = \frac{B_r}{B}, \tag{12}$$

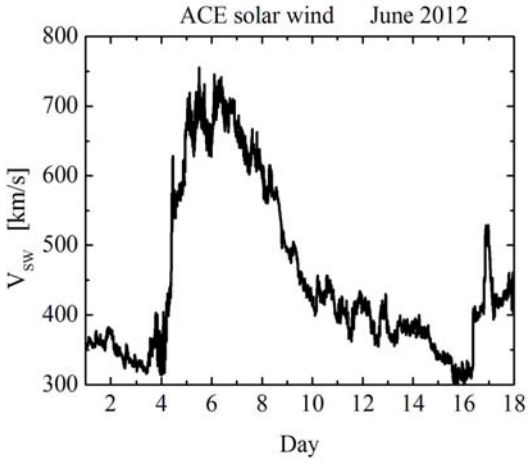

Fig. 5. Solar wind speed from ACE satellite measurements [21], for June 1-18, 2012.

$$\frac{rd\theta}{ds} = \frac{B_\theta}{B}, \tag{13}$$

$$\frac{r\sin\theta d\phi}{ds} = \frac{B_\phi}{B}, \tag{14}$$

where ds is a segment along the field line. Starting from the source surface, we use a fourth-order Runge-Kutta method to trace open magnetic field lines $\mathbf{B}(R_s)$. We find the corresponding foot point $\mathbf{B}(R_0)$ of an open field line to obtain the flux tube expansion factor f_s and separation between open field foot point and its nearest coronal hole boundary θ_b. Using the synoptic magnetogram for June 14, 2012 (15:04UT) as the input and with resolution of the computation set to $2.5^\circ \times 2.5^\circ$, we calculated f_s (Fig. 4a) and θ_b (Fig. 4b). We can associate the solar wind speed to the points at the solar surface using corresponding values for f_s and θ_b (11). For the empirical coefficients in (11) we use $a_1 = 240$, $a_2 = 675$, $a_3 = 1/4.5$, $a_4 = 1$, $a_5 = 0.8$, $a_6 = 2.8$, $a_7 = 1.25$ and $a_8 = 3$ [17]. The result for the solar wind speed is shown in Fig. 4c.

To test the result for the solar wind, in Fig. 5 we plot the solar wind speed observed by the ACE satellite at the L1 point for June 1-18, 2012 [21]. Taking into account that 1 day corresponds to $\approx 13.2^\circ$ in the longitude and accounting for the transition time of the solar wind from R_s to L1 point, we see that the region of the high solar wind speed ($\sim$ 700km/s) in Fig. 4c at $\phi \sim 150$, corresponds to the high solar wind speed ($\sim$ 700km/s) observed around June 6 by the ACE satellite.

We should point out that the original WSA solar wind model [7], [8] uses a simple 1D kinematic relation to propagate the solar wind through the interplanetary space, taking into account overtaking between fast and slow solar wind streams. The WSA prediction of the solar wind can be quite satisfactory during the Sun's quiet period, however, the model often fails to provide satisfactory predictions during periods of increased activity. The reason for this is that the model does not employ a physics based model of the solar wind stream interaction. Moreover, the model does not account for the fast disturbances. To illustrate this, in Fig. 5 we can see two shocks on June 16 due to two CMEs that erupted on June 13 (12:48UT) and June 14 (14:36UT). Although the CMEs were not Earth directed they generated a modest increase in the solar wind speed. However, as one can see, no features associated with this event are present in Fig. 4.

To propagate plasma streams through interplanetary space and to predict shock arrival times of the solar disturbances a large scale MHD model would be appropriate. We are developing a MHD code (similar to ENLIL), where the components used to calculate the coronal field and the solar wind speed in this paper will provide input values at the inner code boundary. Once the MHD propagation code is included in the framework, the fine tuning of empirical coefficients in (11) will be done to best match observations. Furthermore, to take into account the most violent solar disturbances, a CME model will be coupled with the MHD code.

IV. Conclusion

In this paper we presented numerical results based on PFSS coronal field and WSA solar wind models. A good agreement of the results with the observations was found. We plan to couple the developed numerical codes into a framework with an interplanetary MHD and a CME model to simulate propagation of CMEs in the background solar wind.

Acknowledgment

This work utilizes data obtained by the Global Oscillation Network Group (GONG) Program, managed by the National Solar Observatory, which is operated by AURA, Inc. under a cooperative agreement with the National Science Foundation. The data were acquired by instruments operated by the Big Bear Solar Observatory, High Altitude Observatory, Learmonth Solar Observatory, Udaipur Solar Observatory, Instituto de Astrofísica de Canarias, and Cerro Tololo Interamerican Observatory. This work was performed as part of Natural Resources Canada's Public Safety Geoscience program with additional support from the Canadian Space Agency.

References

[1] E. N. Parker, "Suprathermal particle generation in the solar corona," *Astrophys. J.*, vol. 128, p. 677, 1958.
[2] R. Tousey, "The solar corona," in *Space research XIII*, eds. M. J. Rycroft and S. K. Runcorn, Akademie-Verlag, Berlin, 1973, p. 713.
[3] H. Koskinen, and T. Pulkkinen, "State of the art space weather modelling and proposed ESA strategy," *SPEE-WP310-TN*, 1998.
[4] National Space Weather Program Implementation Plan, *FCM-P31-2000*, US, 2002.
[5] National Space Weather Program Strategic Plan, *FCM-P30-2010*, US, 2010.
[6] Space Weather Canada, Natural Resources Canada. http://www.spaceweather.ca
[7] C. N. Arge, and V. J. Pizzo, "Improvement in the prediction of solar wind conditions using near-real time solar magnetic field updates," *Journal of Geophys. Res.*, vol. 105, p. 465, 2000.
[8] C. N. Arge, D. Odstrcil, V. J. Pizzo, and L. R. Mayer, "Improved method for specifying solar wind speed near the Sun," *Solar Wind Ten, Conference Proceedings*, vol. 679, p. 190, 2003.
[9] C. D. Fry *et al.*, "Forecasting solar wind structures and shock arrival times using an ensemble of models," *J. Geophys. Res.* vol. 108, p. 1070, 2003.
[10] Z. Smith, M. Dryer, E. Ort, and W. Murtagh, "Performance of interplanetary shock prediction models," *J. Atmos. Sol.-Terr. Phy.*, vol. 62, p. 1265, 2000.
[11] D. Odstrcil *et al.*, "Initial coupling of coronal and heliospheric numerical magnetohydrodynamic codes," *J. Atmos. Sol.-Terr. Phy.*, vol. 66, p. 1311, 2004.
[12] V. J. Pizzo *et al.*, "Wang-Sheeley-Arge-Enlil cone model transitions to operations," *Space Weather*, vol. 9, p. S03004, 2011.
[13] M. D. Altschuler, and G. Newkirk , "Magnetic field and the structure of the solar corona," *Sol. Phys.*, vol. 9, p. 131, 1969.
[14] M. D. Altschuler *et al.*, "High resolution mapping of the magnetic field of the solar corona," *Sol. Phys.*, vol. 51, p. 345, 1977.
[15] P. Riley *et al.*, "A comparison between global magnetohydrodynamic and potential field source surface model results," *Astrophys. J.*, vol. 653, p. 1510, 2006.
[16] K. H. Schatten, "Current sheet magnetic model for the solar corona," *Cosmic Electrodynamics*, vol. 2, p. 232, 1971.
[17] P. MacNeice, "Validation of community models: 2. Development of a baseline using Wang-Sheeley-Arge model," *Space Weather*, vol. 7, p. S12002, 2009.
[18] National Solar Observatory, Global Oscillation Network Group. http://gong.nso.edu/
[19] NASA. http://heasarc.gsfc.nasa.gov/fitsio/
[20] G. Tóth, B. van der Holst, and Z. Huang, "Obtaining potential field solution with spherical harmonics and finite differences," *Astrophysical Journal*, vol. 732, a. 102, 2011.
[21] Advanced Composition Explorer (ACE). http://www.srl.caltech.edu/ACE/